

# Nano-network electronic conduction in iron and nickel olivine phosphates

P. SUBRAMANYA HERLE, B. ELLIS, N. COOMBS AND L. F. NAZAR\*

University of Waterloo, Department of Chemistry, 200 University Ave. West, Waterloo Ontario Canada N2L 3G1

\*e-mail: lfnazar@uwaterloo.ca

Published online: 22 February 2004; doi:10.1038/nmat1063

**T**he provision of efficient electron and ion transport is a critical issue in an exciting new group of materials based on lithium metal phosphates that are important as cathodes for lithium-ion batteries. Much interest centres on olivine-type  $\text{LiFePO}_4$ , the most prominent member of this family<sup>1</sup>. Whereas the one-dimensional lithium-ion mobility in this framework is high<sup>2</sup>, the electronically insulating phosphate groups that benefit the voltage also isolate the redox centres within the lattice. The pristine compound is a very poor conductor ( $\sigma \sim 10^{-9} \text{ S cm}^{-1}$ ), thus limiting its electrochemical response. One approach to overcome this is to include conductive phases, increasing its capacity to near-theoretical values<sup>3–6</sup>. There have also been attempts to alter the inherent conductivity of the lattice by doping it with a supervalent ion. Compositions were reported to be black p-type semiconductors with conductivities of  $\sim 10^{-2} \text{ S cm}^{-1}$  arising from minority  $\text{Fe}^{3+}$  hole carriers<sup>7</sup>. Our results for doped (and undoped)  $\text{LiMPO}_4$  ( $M = \text{Fe, Ni}$ ) show that a percolating nano-network of metal-rich phosphides are responsible for the enhanced conductivity. We believe our demonstration of non-carbonaceous-network grain-boundary conduction to be the first in these materials, and that it holds promise for other insulating phosphates.

Fascination with the initial report of doped olivine compositions  $\text{Li}_{0.99}\text{D}_{0.01}\text{FePO}_4$  ( $D = \text{Nb, Zr, Mg, Ti}$ ) stemmed not only from their enhanced electrochemical performance, but also from the enormous increase in conductivity seen<sup>7</sup> in samples densified at 800 °C. Nonetheless, the description of a highly electronically conductive phosphate challenges conventional wisdom owing to electronic and structural considerations. Small amounts of carbon contaminant that always arise from the organic iron salt precursors<sup>8</sup> have been considered as a contributing factor to conductivity, and factors based on sources of carbon were suspect<sup>9</sup>. This leads to particularly important thermodynamic considerations. Metal phosphates have a propensity to undergo carbothermal reduction at high temperature. The reaction with  $\text{LiFePO}_4$  and carbon oxidizes the carbon to CO or  $\text{CO}_2$ , and reduces the neighbouring Fe and P ions in the lattice to  $\text{Fe}_2\text{P}$  and/or  $\text{Fe}_3\text{P}$ . We have detected bulk phosphide formation through X-ray diffraction by deliberate addition of carbon 'gel' to the precursors<sup>10</sup>. The addition of carbon has also been used to form  $\text{LiFe}^{\text{II}}\text{PO}_4$  from  $\text{Fe}^{3+}$  precursors, using careful temperature control<sup>11</sup>. High temperatures result in reduction to  $\text{Fe}_2\text{P}$ , whose presence in the bulk at temperatures above 850 °C has been implicated<sup>7</sup>, although it was ruled out as the conductivity source in doped  $\text{LiFePO}_4$  on the basis of microcontact measurements<sup>12</sup>.

We find the carbothermal chemistry can be manipulated through surprisingly subtle variation of the processing conditions and stoichiometry. The nanophase phosphide network that is created in situ within the grain boundaries of the insulating  $\text{LiMPO}_4$  nanocrystallites forms an efficient electrical conduit that can be directly imaged by transmission electron microscopy (TEM). Furthermore, metal phosphates of more easily reduced elements (Ni) in  $\text{LiNiPO}_4$  undergo carbothermal reduction at lower temperatures, and can be rendered conductive through this approach. That electronic transport is first and foremost a consequence of the network, rather than a mixed-valent metal  $\text{M}^{2+/3+}$ , state is suggested by these results.

Our first evidence that a second phase could be responsible for enhanced conductivity came from studies of doped compositions similar to those reported previously<sup>7</sup>. We examined a range of Li compositions  $\text{Li}_x\text{Zr}_{0.01}\text{FePO}_4$ , where  $x$  varies from 0.99 to 0.87, in addition to studying non-Zr-doped samples. Although it is presumed that  $\text{LiFePO}_4$  has a very narrow compositional range, evidence from substituted materials  $\text{Li}_{1-3x}\text{Fe}_x\text{NiPO}_4$  suggests that Li vacancies can be accommodated in the olivine structure<sup>13</sup>. In addition, the doped  $\text{Li}_{0.99}\text{D}_{0.01}\text{FePO}_4$  stoichiometry previously reported<sup>7</sup> for supervalent cations such as  $\text{Zr}^{4+}$  implies a subvalent state of Fe ( $< \text{Fe}^{\text{II}}$ ) on the basis of charge balance (that is, for  $\text{Li}_{0.99}\text{Zr}_{0.01}\text{FePO}_4\text{:Fe}^{+1.97}$ ). Hence, loss of lithium during processing would have to occur to account for  $\text{Fe}^{3+}$  hole carrier formation. Our deliberate departure from Li stoichiometry should introduce  $\text{Fe}^{3+}$  'holes' irrespective of the incorporation of the  $\text{Zr}^{4+}$  dopant. Following the original procedure<sup>7</sup>,  $\text{Li}_x\text{Zr}_{0.01}\text{FePO}_4$  materials ( $x = 0.99 \rightarrow 0.87$ ) were crystallized at 600 °C, pressed to form a dense pellet, and then sintered in argon at 800 °C. The resultant X-ray diffraction (XRD) patterns for powders and pellets are shown in Fig. 1. The materials prepared at 600 °C (Fig. 1a) are almost entirely triphyllite,  $\text{LiFePO}_4$ . Compositions down to  $\text{Li}_{0.93}\text{Zr}_{0.01}\text{FePO}_4$  show reflections due to single-phase  $\text{LiFePO}_4$ . Closer inspection reveals that as the Li content decreases, a slight broadening in the (020) reflection at  $30.3^\circ$  in  $2\theta$  becomes evident, which can be resolved as very weak satellite lines attributable to  $\text{Fe}_2\text{P}_2\text{O}_7$  (Fig. 1a, inset). On heating the pressed pellets to 800 °C the  $\text{Fe}_2\text{P}_2\text{O}_7$  component disappears (Fig. 1b). Mössbauer spectroscopy only revealed the presence of  $\text{Fe}^{2+}$  (Supplementary Information (Fig. S5)). TEM images obtained on microtomed sections of pressed pellets showed a uniform distribution of Zr in the electron energy loss spectra (EELS) map, indicating that the dopant was well dispersed (See Supplementary Information, Fig. S1). Conductivity plots

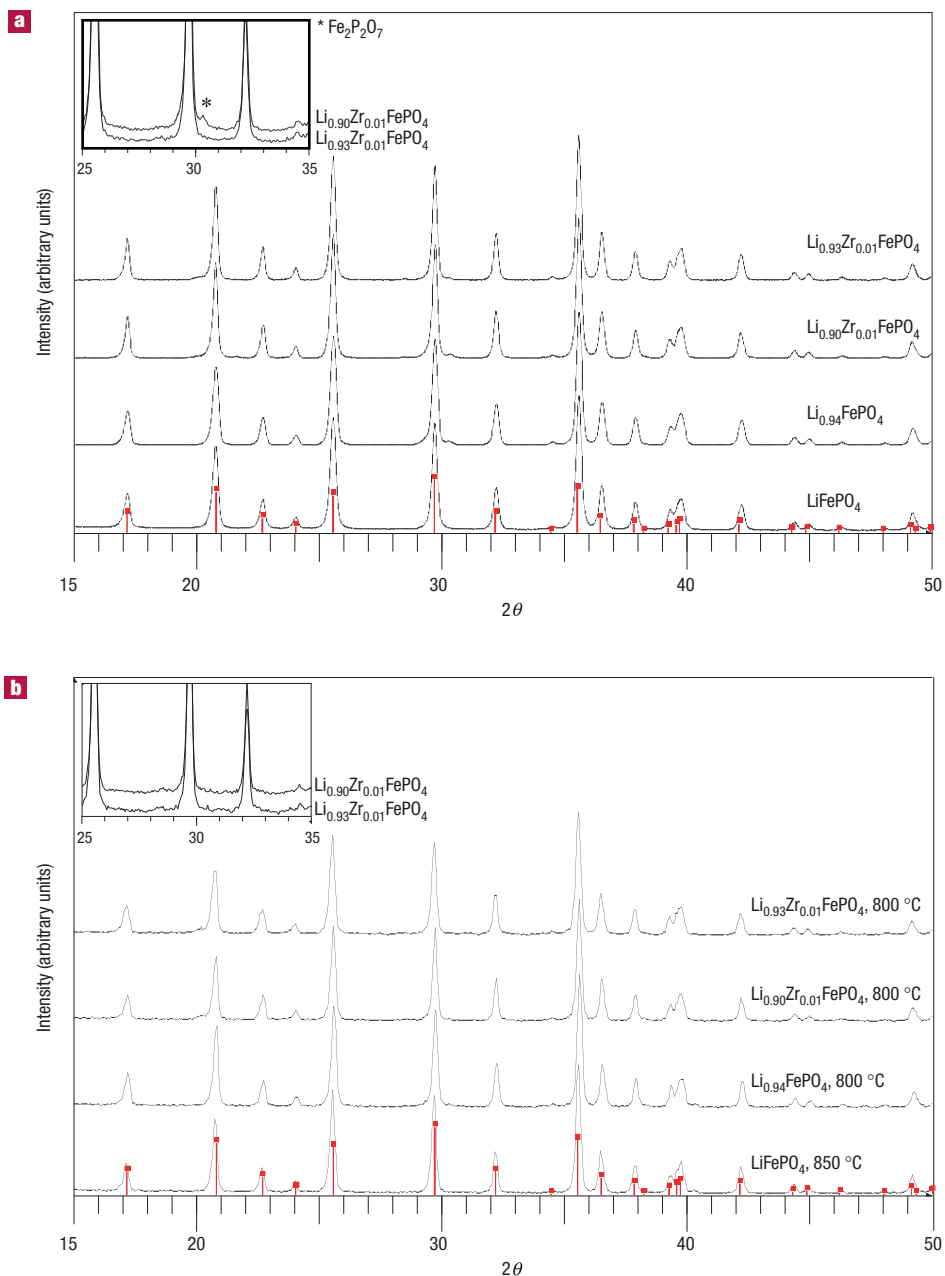


**Figure 1** X-ray diffraction patterns of various powders and sintered pellets of  $\text{Li}_{1-x}\text{Zr}_x\text{FePO}_4$  compositions. Near-single-phase triphylite formation occurs at 600 °C in Li substoichiometric samples, although  $\text{Fe}_2\text{P}_2\text{O}_7$  can be detected in the most Li-deficient samples. This component was not detected after sintering the pellets at elevated temperatures in an argon atmosphere. **a**,  $\text{Li}_{1-x}\text{Zr}_x\text{FePO}_4$  powders prepared at 600 °C; **b**, pellets sintered at 800–850 °C. The reflections of  $\text{LiFePO}_4$  (JCPDS No. 40-1499) are shown on both figures for comparison. We note that a two-phase fit of all of the X-ray data using Rietveld analysis (Supplementary Information, Fig. S2) allowed quantitative assessment of the  $\text{Fe}_2\text{P}_2\text{O}_7$  contribution, showing that it roughly scaled with the substoichiometry as expected. In none of the materials studied, including the Zr-doped samples, was there evidence for solid solution behaviour in  $\text{Li}_{1-x}\text{FePO}_4$  in accord with electrochemical measurements, which show two-phase behaviour on Li extraction to form  $\text{LiFePO}_4 + \text{FePO}_4$  for all compositions  $\text{Li}_{1-x}\text{FePO}_4$ .

for all materials (Fig. 2) demonstrate that very high values are achieved for the densified pellets, with conductivities at 300 K in the range of  $10^{-2}$ – $10^{-3}$   $\text{S cm}^{-1}$ , and activation energies between 30–40 meV. The values are similar to that reported<sup>7</sup> for  $\text{Li}_{0.99}\text{Zr}_{0.01}\text{FePO}_4$ , although the latter did not show appreciable conductivity in our work. The room-temperature value for the composition  $\text{Li}_{0.96}\text{Zr}_{0.01}\text{FePO}_4$  was estimated as  $10^{-5}$   $\text{S cm}^{-1}$ . The conductivity generally increases with decreasing

lithium stoichiometry, albeit with some variability due to changes in the processing conditions.

A TEM image of an ultramicrotomed slice taken from a conductive composition,  $\text{Li}_{0.90}\text{Zr}_{0.01}\text{FePO}_4$ , is shown in Fig. 3a and corresponding Fe, Li and C maps are displayed in Fig. 3b–d. Together, these show clear evidence of the formation of two distinct nanophases. The regions between the darker  $\text{LiFePO}_4$  crystallites (20–100 nm in size) in the

micrograph appear as black domains in the Fe, Li EELS maps. Particularly startling is the carbon map (Fig. 3d), which reveals that the edges of the  $\text{LiFePO}_4$  crystallites are coated with a carbon-containing layer between 5 and 10 nm thick, and which forms a network connecting all of the particles and completely filling some of the voids. X-ray fluorescence analysis (EDX) of the regions nearest the grain boundaries gave an Fe/P ratio close to 2:1 (65:35), whereas analysis of the bulk provided an Fe/P ratio of close to 1:1 (45:55), identical to a 'control' sample of non-conducting  $\text{LiFePO}_4$  densified at 800 °C (Fig. 4, and Supplementary Information, Fig. S3). Thus,  $\text{Fe}_2\text{P}$  and/or iron phosphocarbide,  $\text{Fe}_{75}\text{P}_{15}\text{C}_{10}$ , is formed by carbothermal reduction of the  $\text{LiFePO}_4$  with carbon at and within the grain boundaries. Some carbon, arising from both the oxalate precursor and alkoxide in the Zr-dopant, may remain in partially graphitized form. The phosphocarbide is an amorphous, magnetic phase intermediate between  $\text{Fe}_3\text{P}$  and  $\text{Fe}_3\text{C}$  (ref. 14), with a conductivity of about  $10^{-1} \text{ S cm}^{-1}$ , similar to that of  $\text{Fe}_2\text{P}$  (ref. 15). Their existence gives rise to the observed bulk conductivity in these Zr-doped Li-deficient materials.

Further evidence that these grain-boundary 'nano-networks' can act as efficient electrical conduits comes from our examination of non-Zr doped materials. Samples of  $\text{Li}_x\text{FePO}_4$  ( $x = 0.91$  to 1.00) were prepared using the same process, without the dopant. The values of  $x$  were 'valent-equivalent' to the Zr-doped samples described above, where the total valence contribution of  $x(\text{Li}^+) + 0.01\text{Zr}$  was kept constant. As in the Zr-doped materials, phase separation to stoichiometric  $\text{LiFePO}_4$  and a minor amount of  $\text{Fe}_2\text{P}_2\text{O}_7$  occurred on crystallization of the precursors at 600 °C, as shown by XRD (for Reitveld analysis of phase fraction, see Supplementary Information, Fig. S2). A representative pattern is shown for  $\text{Li}_{0.94}\text{FePO}_4$  in Fig. 1. The fraction of  $\text{Fe}_2\text{P}_2\text{O}_7$  correlates with 'x' as expected, and disappears from the pattern at 800 °C (Fig. 1b, inset). Samples pressed at high pressure and heated at 800 °C showed excellent conductivity, achieving the same values as the Zr-doped materials (Fig. 2). Carbon content in  $\text{LiFePO}_4$  arises from decomposition of the iron oxalate, whereas in the Zr-doped materials, the alkoxide also contributes carbon (12 mol% for the precursor): nonetheless the conductivity of  $\text{Li}_{0.90}\text{Zr}_{0.01}\text{FePO}_4$  (800 °C) and  $\text{Li}_{0.94}\text{FePO}_4$  is not substantially different. Samples of  $\text{Li}_x\text{FePO}_4$  prepared from non-carbon-containing precursors ( $\text{Fe}_3(\text{PO}_4)_2 \cdot 8\text{H}_2\text{O} + \text{Li}_3\text{PO}_4$ ) were not conductive ( $\sigma < 10^{-7} \text{ S cm}^{-1}$ ) at any temperature. Stoichiometric  $\text{LiFePO}_4$  (iron oxalate precursor) subjected to heat treatment at 800 °C was also essentially non-conductive, with a value less than  $10^{-7} \text{ S cm}^{-1}$  in accordance with previous reports. However, the conductivity of that sample treated at a slightly higher temperature of 850 °C rose very sharply (Fig. 2), and even exceeded that of the substoichiometric materials to achieve values of about  $10^{-2} \text{ S cm}^{-1}$ . Carbon from oxalate decomposition is present at both 800 and 850 °C. We conclude that (i) iron phosphide and/or iron phosphocarbide at the grain boundaries, not carbon, is primarily responsible for the grain-boundary transport; and (ii) reduction to the phosphide occurs at lower temperatures in substoichiometric  $\text{Li}_{1-x}\text{FePO}_4$  than in its undoped, stoichiometric counterpart. This may be explained by more facile reduction of  $\text{Fe}_2\text{P}_2\text{O}_7$  to form iron phosphide, which occurs at a lower temperature than  $\text{LiFePO}_4$ .

These results suggest that the concept can be extended to other phosphates,  $\text{LiMPO}_4$  ( $M = \text{Ni, Mn, Co}$ ) that have a higher oxidation potential than  $M = \text{Fe}$ . Samples of  $\text{Li}_x\text{NiPO}_4$  ( $x = 0.94$  to 1.00) were prepared similarly to the iron phosphates, except that the atmosphere and temperature of heat treatment was varied. Unlike  $\text{LiFePO}_4$ , which oxidizes to Fe(III) in air at elevated temperatures,  $\text{LiNiPO}_4$  is stable in oxygen at high temperature<sup>16</sup>, which affords unequivocal confirmation of the carbothermal chemistry. These conditions favour formation of a potentially mixed-valent  $\text{Ni}^{2+/3+}$  hole-conductor state, but would oxidize conductive nickel phosphides. Preparation of  $\text{Li}_x\text{NiPO}_4$  by heating carbon-containing precursors at temperatures between 600 and 900 °C in air or oxygen yielded bright-yellow crystalline powders

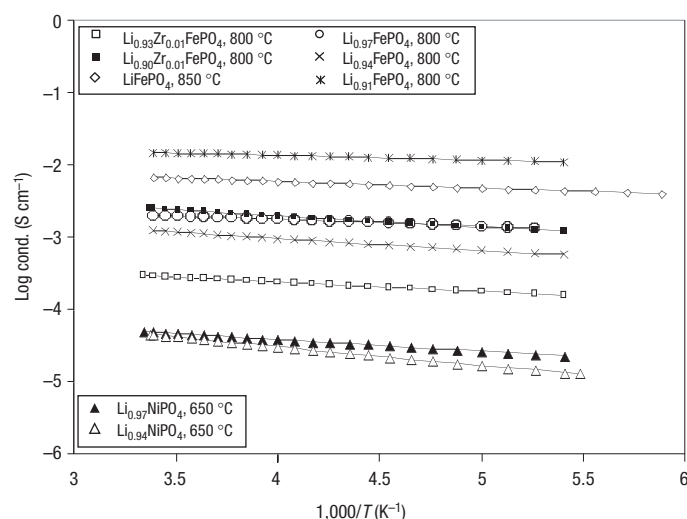


**Figure 2** Conductivity of  $\text{Li}_{1-x}\text{Zr}_x\text{MPO}_4$  ( $M = \text{Fe, Ni}$ ) samples. High conductivity is observed for all samples irrespective of dopant content. All compositions can be made conductive over the temperature range from 300 K to 180 K by choosing suitable sintering temperatures and compositions, showing values in excess of  $10^{-3} \text{ S cm}^{-1}$  for iron compositions and  $10^{-5} \text{ S cm}^{-1}$  for the nickel compositions at room temperature. Results are for pellets sintered between 650 °C and 850 °C and measured by four-point probe d.c. methods. For the nickel sample, carbothermal reaction is not initiated below 600 °C, but above this temperature the reaction is sufficiently vigorous that the nucleation of a few larger  $\text{Ni}_3\text{P}$  crystallites ensues. These migrate outside the grain boundaries, resulting in a drop in the overall transport efficiency. We note that heat treatment of  $\text{Li}_x\text{NiPO}_4$  above 650 °C results in non-conductive light-grey expanded pellets; CO or  $\text{CO}_2$  is released by rapid consumption of carbon, resulting in volume expansion and loss of contact between conducting paths. The iron compound, having a lower oxidation potential, provides a wider temperature window for initiation of metal phosphide production before excessive carbothermal reduction takes place (above 925 °C).

for all compositions  $x$ . All were non-conductive ( $\sigma < 10^{-7} \text{ S cm}^{-1}$ ). For  $x = 1$ , the diffraction pattern (Supplementary Information, Fig. S4) showed that stoichiometric  $\text{LiNiPO}_4$  was formed; for  $x < 1$ ,  $\text{Li}_4\text{P}_2\text{O}_7$  and  $\text{Ni}_2\text{P}_2\text{O}_7$  were minor contaminants. By contrast, heat treatment under argon at 600 °C resulted in deep black materials consisting of  $\text{LiNiPO}_4$ , and minor fractions of  $\text{Ni}_3\text{P}$  (along with  $\text{Li}_4\text{P}_2\text{O}_7$  and  $\text{Li}_2\text{Ni}_3\text{P}_4\text{O}_{14}$ ). Conductivity measurements of a pressed sintered (650 °C) pellet of these materials showed values of about  $10^{-4} \text{ S cm}^{-1}$  at room temperature (Fig. 2). That this conductivity is lower than the corresponding iron phosphates is owing to the lower densification temperature, and differences in the energetics of phosphate decomposition.  $\text{Li}_x\text{NiPO}_4/\text{C}$  undergoes vigorous carbothermal reaction to form CO/ $\text{CO}_2$  at the same temperature at which carbothermal chemistry for Fe just commences. This more facile reduction corresponds to a greater thermodynamic driving force, arising from the easier reduction of  $\text{Ni}^{\text{II}}$  in  $\text{LiNiPO}_4$  versus  $\text{Fe}^{\text{II}}$  in  $\text{LiFePO}_4$ . The kinetics of these reactions is also affected by the mechanism of phosphide formation. These mechanisms remain to be fully understood for Ni (and Fe) and will be addressed in subsequent studies.

Metal phosphide formation not only explains the conductivity of the  $\text{LiFePO}_4$  and  $\text{LiNiPO}_4$  materials at high temperatures, but also the magnetic behaviour of the composite materials. In our iron phosphate materials, conductivity of the composites formed at 800–850 °C was associated with easily detectable ferromagnetism of the samples, despite the antiferromagnetism of  $\text{LiFePO}_4$  (ref. 17). The ferromagnetic properties of the iron phosphides, ( $\text{Fe}_2\text{P}$ ,  $\text{Fe}_3\text{P}$  and  $\text{Fe}_{75}\text{P}_{15}\text{C}_{10}$ ; refs 15, 18

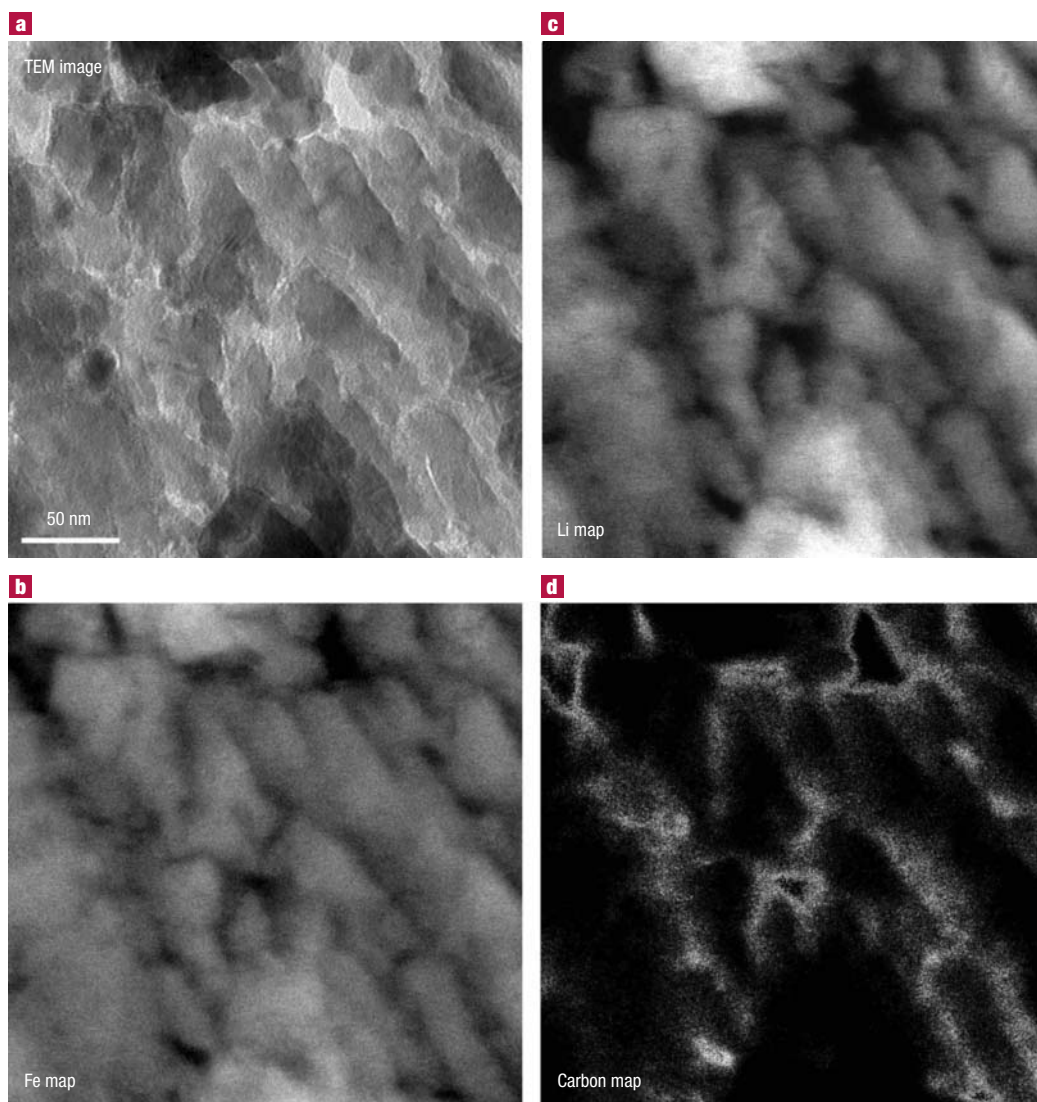


**Figure 3** Elemental mapping of  $\text{Li}_{0.90}\text{Zr}_{0.01}\text{FePO}_4$ . **a–d**, The elemental Fe (**b**), Li (**c**) and C (**d**) maps, generated by EELS mapping of the TEM micrograph shown in **a**, illustrate the network formation of carbon and  $\text{Fe}_2\text{P}$  in the interstitial grain-boundary region. In the micrograph, the  $\text{LiFePO}_4$  crystallites appear as the darker regions, with differing intensity indicating variation in crystallite thickness. The irregularly shaped particles are clearly illustrated by the corresponding bright domains in the Fe and Li EELS maps. The regions between the crystallites (20–100 nm in size) and their edges appear as black domains in the EELS maps and as lighter areas in the micrograph. The scale refers to all the images.

and 14, respectively) account for this behaviour. It also explains the previously reported magnetization of (sintered)  $\text{LiFePO}_4$  samples noted in Hall measurements<sup>7</sup>. Moreover, although the electronic conductivity of the nickel phosphate is directly associated with nickel phosphide formation, the non-magnetic nature of these materials is consistent with the paramagnetic nature of  $\text{Ni}_3\text{P}$  (ref. 19).

Particularly important is that the grinding procedure used to form these composites gives rise to efficient coating of the carbon precursors responsible for the reduction at the crystallite surface, and beneficially reduces the crystallite size of the particles. We anticipate that the same process should be readily extendable to other olivines such as  $\text{LiMnPO}_4$  and  $\text{LiCoPO}_4$ , and also to other phosphates. Adroit choices of processing conditions and composition may result in formation of conductive networks at even lower temperatures. Selectively manipulating the reactivity of these materials can also be envisioned to form in situ nano-networks that are applicable not only for energy storage applications, but a range of other useful physical properties that derive

from the combination of insulating and conductive/magnetic materials at the nanoscale level.

## METHODS

### SYNTHESIS

Powders were synthesized using  $\text{Li}_2\text{CO}_3$  (99.999%, Alfa Aesar),  $\text{FeC}_2\text{O}_4 \cdot 2\text{H}_2\text{O}$  (99.999%, Alfa Aesar) (or  $\text{NiC}_2\text{O}_4 \cdot 2\text{H}_2\text{O}$ , 99%, Alfa Aesar) and  $\text{NH}_4\text{H}_2\text{PO}_4$  (99.998%, Alfa Aesar) as the precursor reagents; where Zr doping was used, it was introduced as  $\text{Zr}(\text{OC}_2\text{H}_5)_4 \cdot \text{C}_2\text{H}_5\text{OH}$  (Alfa Catalogue Chemicals). Stoichiometries of the reagents were adjusted to prepare the formulations described in the text. The precursors were ball-milled for between 6 and 18 h in silicon nitride media in acetone, removed from the mill and dried, and ground in an argon-filled glove box using an agate mortar and pestle. In a typical preparation of the iron phosphates, 3–4-g batches of the powders were first heated to 350 °C for 10 h in flowing argon (200 ml min<sup>-1</sup>) using a fine titanium metal getter in the gas stream to control oxygen activity), followed by heat treatment at 600 °C for up to 8 h. Pellets were pressed (5 tons) from ~200 mg of the powder and sintered at either 800 or 850 °C for 10 h. In most cases, pellets were covered with powder of the same composition. A weight loss of about 1.5–2% in the pellets was consistently observed after sintering, which we attributed to evolution of  $\text{CO}/\text{CO}_2$  and/or  $\text{Li}_2\text{O}$ . Samples of  $\text{Li}_x\text{FePO}_4$  from non-carbon-containing precursors were made by reacting vivianite with  $\text{Li}_3\text{PO}_4$  following literature procedures<sup>20</sup>,

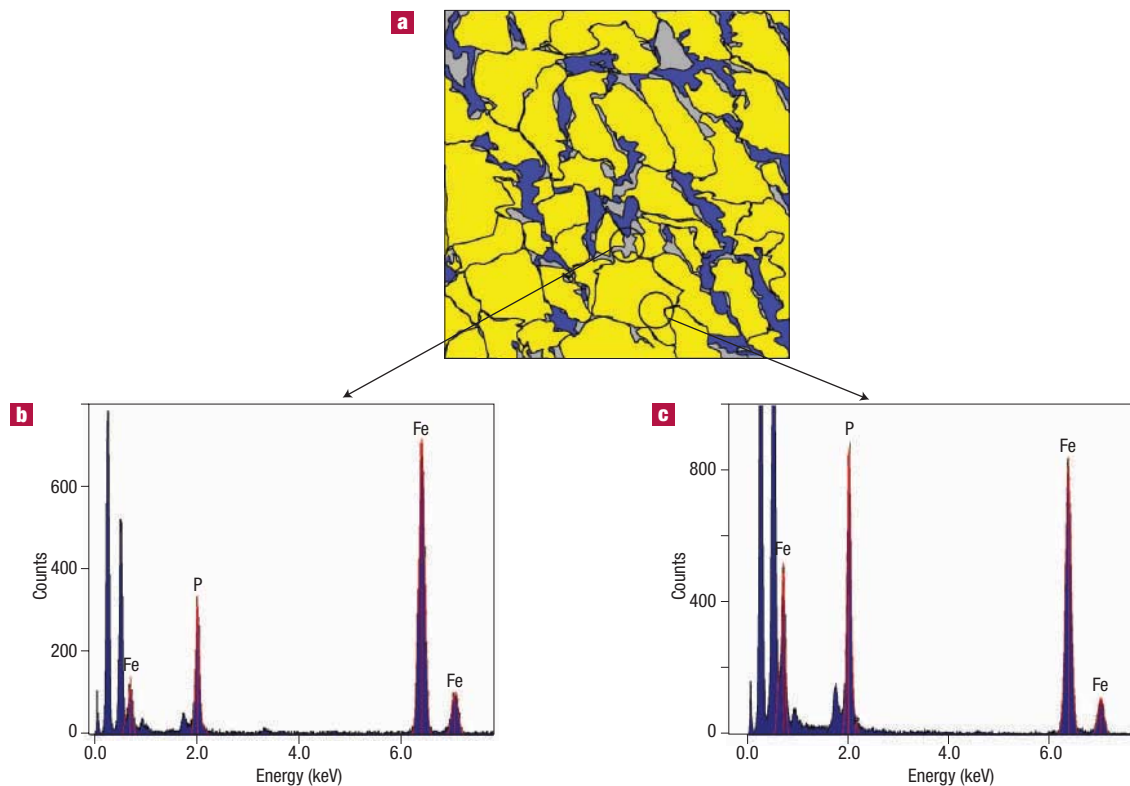


**Figure 4** Representation of the  $\text{Li}_{1-x}\text{Zr}_{0.01}\text{FePO}_4$  composite. **a**, The schematic, generated from the image and superposition of the Fe and C elemental maps depicted in Fig. 3, shows the location of  $\text{Fe}_2\text{P}$ , C and carbon in the interstitial grain-boundary region ( $\text{LiFePO}_4$ ; yellow;  $\text{C}/\text{Fe}_{75}\text{P}_{15}\text{C}_{10}$ ; blue;  $\text{Fe}_2\text{P}$ ; grey). The corresponding EDX analysis of the grain-boundary (**b**) and bulk (**c**) regions confirm that the Fe/P ratio of 1:1 is preserved in the bulk, but is close to 2:1 in the grain boundaries. The area fraction of the grain-boundary material is estimated at 5%. The overall semiconducting behaviour observed in Fig. 2 is accounted for by the conductivities of the intergranular materials: (amorphous carbon)<sup>21</sup>;  $3.3 \times 10^{-1} \text{ S cm}^{-1}$  ( $\text{Fe}_2\text{P}$  single crystal)<sup>18</sup>;  $5.2 \times 10^{-2} \text{ S cm}^{-1}$  ( $\text{Fe}_2\text{P}$ , pressed powders)<sup>10</sup> and  $\sim 10^{-1} \text{ S cm}^{-1}$  ( $\text{Fe}_{75}\text{P}_{15}\text{C}_{10}$ )<sup>22</sup>.

using stoichiometries  $(1-0.33x) \text{Li}_3\text{PO}_4:(0.33x) \text{NH}_4\text{H}_2\text{PO}_4:\text{Fe}_3(\text{PO}_4)_2 \cdot 8\text{H}_2\text{O}$ . For preparation of the conductive nickel phosphates, the powders were first heated to 350 °C for 10 h in flowing argon, followed by heat treatment at 600 °C for 8 h and sintering of the densified pellet at 650 °C for an additional 10 h. Samples of the non-conductive  $\text{Li}_x\text{NiPO}_4$  materials were prepared under the same conditions with the exception of using flowing air as the atmosphere for some experiments.

#### XRD AND TEM

XRD was performed on a Bruker D8-Advantage powder diffractometer using  $\text{Cu-K}\alpha$  radiation (wavelength  $\lambda = 1.5405 \text{ \AA}$ ) from  $2\theta = 10$  to 80 degrees at a count rate of 1 s per step of 0.02°. TEM analysis was carried out by embedding a small portion of the sintered pellet in epoxy resin, and slicing the sample with an ultramicrotome. The slice was mounted on thin carbon films supported on a 200-mesh copper grid. TEM imaging and conventional EDX analysis at the grain-boundary region was performed using a Technia 20 instrument (FEL, USA) operating at 200 kV accelerating voltage. EELS maps were generated using a Gatan energy filter (GIF-2000). EDX spot elemental analysis was also performed on the same slice using a Hitachi S5200 operating at 30 kV in STEM mode to confirm the Fe/P ratios (see Supplementary Information, Fig. S3).

#### CONDUCTIVITY MEASUREMENTS

Pellet surfaces were polished before variable temperature conductivity measurements, which were performed using four-point d.c. methods. Electrode contacts were affixed using silver or gold paste in linear geometry on a thin section of a pellet of approximate dimensions:  $1 \text{ mm} \times 1 \text{ mm} \times 5 \text{ mm}$ . The activation energies were calculated using the expression  $\sigma = \sigma_0 e^{-E_a/kT}$ .

Received 21 October 2003; accepted 15 December 2003; published 22 February 2004.

#### References

1. Padhi, A. K., Nanjundaswamy, K. S. & Goodenough, J. B. Phospho-olivines as positive electrode materials for rechargeable lithium batteries. *J. Electrochem. Soc.* **144**, 1188–1194 (1997).
2. Morgan, D., van der Zee, A. & Ceder, G. Li ion conductivity in  $\text{Li}_x\text{MPO}_4$  ( $\text{M} = \text{Mn, Fe, Co, Ni}$ ) olivine materials. *Electrochem. Solid State Lett.* **7**, A30–A32 (2004).
3. Ravet, N. *et al.* Improved iron based cathode material. Abstract No. 127, *Electrochemical Society Fall Meeting*, Honolulu, Hawaii (Electrochemical Society, Pennington, New Jersey, 1999).
4. Li, G., Yamada, A. & Azuma, H. Method for manufacturing active material of positive plate and method for manufacturing non-aqueous electrolyte secondary cell. European Patent EP 1,094,532A1 (2001).
5. Huang, H., Yin, S.-C. & Nazar, L. F. Approaching theoretical capacity of  $\text{LiFePO}_4$  at room temperature at high rates. *Electrochem. Solid State Lett.* **4**, A170–A172 (2001).
6. Croce, F. *et al.* A novel concept for the synthesis of an improved  $\text{LiFePO}_4$  lithium battery cathode. *Electrochem. Solid State Lett.* **5**, A47–A50 (2002).
7. Chung, S.-Y., Bloking, J. T. & Chiang, Y.-M. Electronically conductive phospho-olivines as lithium storage electrodes. *Nature Mater.* **1**, 123–128 (2002).
8. Doeff, M. M., Hu, Y., McLarnon, F. & Kostecki, R. Effect of surface carbon structure on the electrochemical performance of  $\text{LiFePO}_4$ . *Electrochem. Solid State Lett.* **6**, A207–A209 (2003).
9. Ravet, N., Abouimrane, A. & Armand, M. Correspondence. *Nature Mater.* **2**, 702 (2003).
10. Ellis, B., Herle, P. S. & Nazar, L. F.  $\text{LiFePO}_4$  and its doped derivatives. Abstract No. 1074, 203rd *Electrochemical Society Spring Meeting*, Paris (Electrochemical Society, Pennington, New Jersey, 2003).
11. Barker, J., Saidi, M. Y. & Swoyer, J. L. Lithium iron(II) phospho-olivines prepared by a novel carbothermal reduction method. *Electrochem. Solid State Lett.* **6**, A53–A55 (2003).
12. Chung, S.-Y. & Chiang, Y.-M. Microscale measurements of the electrical conductivity of doped  $\text{LiFePO}_4$ . *Electrochem. Solid State Lett.* **6**, A278–A281 (2003).
13. Goni, A., Arriortua, M. I., Barberis, G. E. & Rojo, T. Unexpected substitution in the  $\text{Li}_{1-x}\text{Fe}_x\text{NiPO}_4$  solid solution. Weak ferromagnetic behaviour. *J. Mater. Chem.* **10**, 423–428 (2000).
14. Berry, B. S. & Pritchard, W. C. Temperature dependence of the  $\Delta E$  effect in amorphous  $\text{Fe}_{75}\text{P}_{15}\text{C}_{10}$ . *Solid State Commun.* **26**, 827–829 (1978).
15. Fujii, H., Hokabe, T., Kamigai, T. & Okamoto, T. Magnetic properties of iron phosphide ( $\text{Fe}_2\text{P}$ ) single crystal. *J. Phys. Soc. Jpn* **43**, 41–46 (1977).
16. Garcia-Moreno, O. *et al.* Influence of the structure on the electrochemical performance of lithium transition metal phosphates as cathodic materials in rechargeable lithium batteries: A new high-pressure form of  $\text{LiMPO}_4$  ( $\text{M} = \text{Fe}$  and  $\text{Ni}$ ). *Chem. Mater.* **13**, 1570–1576 (2001).
17. Rousse, G., Rodriguez-Carvajal, J., Patoux, S. & Masquelier, C. Magnetic structures of the triphylite  $\text{LiFePO}_4$  and of its delithiated form,  $\text{FePO}_4$ . *Chem. Mater.* **15**, 4082–4090 (2003).

18. Meyer, A. J. P. & Cadeville, M. C. Magnetic properties of iron-phosphorus compounds. *J. Phys. Soc. Jpn* **17**, 223–225 (1962).
19. Zeppenfeld, K. & Jeitschko, W. Magnetic behaviour of  $\text{Ni}_3\text{P}$ ,  $\text{Ni}_2\text{P}$ ,  $\text{NiP}_3$  and the series  $\text{Ln}_2\text{Ni}_{12}\text{P}_7$ . *J. Phys. Chem. Solids* **54**, 1527–1531 (1993).
20. Herstedt, M. *et al.* Surface chemistry of carbon-treated  $\text{LiFePO}_4$  particles for Li-ion battery cathodes studied by PES. *Electrochem. Solid State Lett.* **6**, A202–A206 (2003).
21. Dimitriadis, C. A., Hastas, N. A., Vouroutzis, N., Logothetidis, S. & Panayiotatos, Y. Microstructure and its effect on the conductivity of magnetron sputtered carbon thin films. *J. Appl. Phys.* **89**, 7954–7959 (2001).
22. Axe, J. D., Passell, L. & Tsuei, C. C. Spin waves in an amorphous metallic ferromagnet,  $\text{Fe}_{73}\text{P}_{15}\text{C}_{10}$ . *AIP Conf. Proc.* **24**, 119–120 (1974).

## Acknowledgements

We gratefully acknowledge funding from the National Sciences and Engineering Research Council of Canada (NSERC) through its Discovery Grant Program. We also thank R. A. Dunlap (Physics, University of Dalhousie) for providing the Mössbauer data. We gratefully acknowledge the help of Ian Swainson (Chalk River Neutron Beam Laboratory) in acquiring neutron diffraction data on substoichiometric  $\text{Li}_x\text{FePO}_4$ .

Correspondence and requests for materials should be addressed to L.E.N.

Supplementary Information accompanies the paper on [www.nature.com/naturematerials](http://www.nature.com/naturematerials)

## Competing financial interests

The authors declare that they have no competing financial interests.